JOURNAL OF GEOPHYSICAL RESEARCH, VOL. 94, NO. B9, PAGES 12,463–12,481, SEPTEMBER 10, 1989

COMPRESSIBLE CONVECTION WITH CONSTANT AND VARIABLE VISCOSITY: THE EFFECT ON SLAB FORMATION, GEOID, AND TOPOGRAPHY

Harro Schmeling

Uppsala University, The Hans Ramberg Tectonic Laboratory, Department of Mineralogy and Petrology, Institute of Geology, Uppsala, Sweden

Abstract. Two-dimensional, Cartesian finite difference models of compressible convection with constant and variable viscosity and fixed bottom temperature are presented. Density variations according to the Adams Williamson equation of state are included. In the case of constant viscosity convection, viscous and adiabatic heating damp the flow. Compressible density variations hardly influence geoid undulations; however, the lower thermal boundary layer becomes thinner, and the mean cell temperature increases. In the case of variable viscosity, the nonlinear coupling between compression, adiabatic and viscous heating, and a temperature-, pressure-, and stress-dependent rheology leads to important consequences: The upwelling flow broadens and plumes are retarded. The flow strongly concentrates toward the downwelling region and becomes mechanically decoupled from the interior of the cell by a low-viscosity region. This mechanism seems to be important for the formation of subducting slabs. Extrapolated to mantle conditions, two low-viscosity regions are predicted flanking the slab on either side and inhibiting an early dispersal and mixing of slab material into the mantle. This process might be aided by an increase of negative buoyancy forces with depth as observed in the models. Further results are as follows: Increasing the dissipation number in variable viscosity convection may either damp or speed up convection, depending on the rheology. Models with internal heating and a fixed bottom temperature show that the threshold to time-dependent variable viscosity convection is drastically reduced if the anelastic liquid approximation is applied instead of the extended Boussinesq approximation.

1. Introduction

Although great advances have been made in exploring the three-dimensional structure of the Earth mantle (e.g., Dziewonski, 1984; Morelli and Dziewonski, 1987), we are far from completely understanding the dynamics of mantle convection. A major unresolved question is the role of the lithosphere (e.g., Davies, 1988) and its fate after subduction (e.g., Craeger and Jordan, 1986; Kincaid and Olson, 1987). It is well known that one of the keys to this question might be the non-Newtonian, temperature- (T) and pressure-(P)dependent rheology appropriate to silicates at moderate to high stresses (e.g., Ranalli, 1987). Recently, it has been recognized that thermal and mechanical effects arising from compression in the mantle also strongly influence the behavior of convection due to interaction with a (T,P)-dependent rheology (e.g., Yuen et al., 1987). The main purpose of this paper is to explore such interaction more in detail assuming also non-Newtonian rheology and examining the flow fields.

There have been several attempts to simulate mantle convection including moving lithospheric plates. Laboratory models using parafin (Jacoby, 1976; Jacoby and Schmeling, 1981) and glucose solutions (Kincaid and Olson, 1987) successfully simulated the subduction of a cold stiff sheet but never reached a steady state, in which new lithosphere is continuously formed by cooling at the surface. In numerical simulations, steady state convection with lithosphere formation and subduction was obtained by artificially introducing stiff lids with local weak zones (Kopitzke, 1979; Jacoby and Schmeling, 1982). Other modellers assumed complex rheological laws in order to allow the "lithosphere" to subduct without being retarded and dispersed by the high viscosities associated with cold downwelling material (Schmeling and Jacoby, 1981; Cserepes, 1982; Christensen and Yuen, 1984). Schmeling and Jacoby (1981) observed that moderate viscous dissipation and adiabatic heating may aid the subduction of "slabs". It will be demonstrated in this study, that strong viscous and adiabatic heating appropriate for compressible mantle convection in connection with a simple temperature-, pressure-, and stress-dependent rheology will mechanically decouple the downwelling flow from the ambient mantle, leading to the formation of flow structures similar to subducting slabs.

Among the enormous amount of mantle convection models carried out in the last 25 years, only few have assumed a non-Newtonian, (T,P)-dependent rheology. Often the use of Newtonian rather than non-Newtonian rheology was justified by an empirical law found by Christensen (1983). For incompressible fluids he showed that the properties of non-Newtonian convection can be closely imitated by a Newtonian fluid with a reduced value of the activation enthalpy of the temperature- and pressure-dependent viscosity. In this study it will be tested if this correspondence holds if the effects of compression are included.

It has long been recognized that compression within a convective mantle leads to the combined effect of adiabatic and viscous heating (Turcotte et al., 1974), both of which are measured by the same nondimensional number, the Dissipation number Di

Paper number 89JB00544.
0148-0227/89/89JB-00544$05.00

$$Di = \frac{hg\alpha}{c_p} \quad (1)$$

where h is the thickness of the convecting layer, g the gravity acceleration, α the thermal coefficient of volumetric expansion, and c_p the specific heat at constant pressure. Increasing Di establishes an adiabatic temperature gradient and decreases the vigor of constant viscosity convection. However, the coupling of adiabatic and viscous heating with a temperature-dependent rheology leads to a more complex behavior. For example, Zhao and Yuen (1987) found a decrease in the vigor of penetrative convection with increasing Di, while Quareni and Yuen (1988) presented mean field solutions with increasing convective vigor. Obviously, such differences are due to different modes of heating and rheological parameters.

In addition to the thermal effect, compressibility influences the dynamics of convection mechanically due to varying density according to the equation of state. In the case of whole mantle convection, fluid particles undergo compressible density changes of up to 60% of the surface density (cf. PREM (Dziewonski and Anderson, 1981)). Jarvis and McKenzie (1980) first included the Adams Williamson equation of state in the equations of convection. The mechanical effect of compressibility can be measured by the parameter combination Di/γ, where the Grüneisen parameter γ (which can be regarded as a nondimensional incompressibility) is defined as

$$\gamma = \frac{\alpha K_S}{\rho c_p} = \frac{\alpha K_T}{\rho c_S} \quad (2)$$

where ρ is the density and K is the incompressibility; subscripts S and T denote constant entropy and temperature, respectively.

It took a number of years until the compressible approach was adopted by other convection modellers (e.g., Bercovici et al., 1988; Solheim and Peltier, 1988; Machetel and Yuen, 1988; Machetel and Yuen, in press, 1989). However, only few have focused on the role of γ (Quareni and Yuen, 1987). In such calculations it turned out that not only increasing Di but also decreasing γ (i.e., increasing compressibility) increases the mean mantle temperature. The coupling between the thermodynamic parameters of the equation of state and the rheology in a convecting mantle were used by Yuen et al. (1987) and Yuen and Zhang (1989) to determine upper bounds of the activation energy and volume in the mantle.

The objective of this work is to study the role of compression in a convecting mantle with special attention to variable viscosity. Rather than choosing Di and γ as close to the realistic value as possible, a whole range of values will be explored (in one case, far beyond the geophysically reasonable value). With respect to other assumptions, it seems permissible to choose the models as simple as possible. The assumptions include two dimensionality, a square box, and rheology laws yielding effective Rayleigh numbers of the order of 10^6.

Since compressibility leads to density variations, one might expect that the geoid of a convecting mantle is influenced by Di and γ. In section 3.1, constant viscosity convection models will, however, demonstrate that there is only a weak dependence on Di and virtual no dependence on γ. While the above mentioned compressible, variable viscosity calculations all used the mean field approach, which gives only vertical profiles of the interesting parameters, two-dimensional models will be presented in section 3.2. Special emphasis will be placed on flow geometry, magnitude, and slab formation. The effect of localized adiabatic and viscous heating on a temperature-dependent viscosity will be studied. Further points of interest will be the thickness of the thermal boundary layer and the time dependence of compressible convection.

2. Mathematical Formulation

The equations of mass, momentum, and energy are given (e.g. Schmeling and Jacoby, 1981):

$$\frac{\partial \rho}{\partial t} + \nabla \rho \vec{v} = 0 \quad (3)$$

$$\rho \left[\frac{\partial \vec{v}}{\partial t} + (\vec{v}\nabla)\vec{v} \right] = -\nabla P + \frac{\partial}{\partial x_j} \tau_{ji} + \rho \vec{g} \quad (4)$$

$$\rho c_P \left[\frac{\partial T}{\partial t} - \frac{\alpha (T+T_o)}{\rho c_P} \frac{\partial P}{\partial t} + \vec{v}(\nabla T - (\nabla T)_s) \right]$$

$$= \nabla k \nabla T + \tau_{ij} \frac{\partial v_i}{\partial x_j} + \rho H \quad (5)$$

where t is the time, $\vec{v}$ the flow velocity, P the pressure, τ_{ij} the deviatoric stress tensor, T the absolute temperature minus the temperature T_o at the top of the convecting layer, k is the thermal conductivity, and H is the rate of internal heating per mass. The stress is related to the velocity field by the constitutive equation

$$\tau_{ij} = \eta \left| \frac{\partial v_i}{\partial x_j} + \frac{\partial v_j}{\partial x_i} - \frac{2}{3} (\nabla \vec{v}) \delta_{ij} \right| + \eta_b (\nabla \vec{v}) \delta_{ij} \quad (6)$$

where η is the dynamic (shear) viscosity, η_b the bulk viscosity, δ_{ij} the Kronecker delta. Following Jarvis and McKenzie (1980), the equation of state can be written as a linear Taylor expansion of ρ about a reference density ρ_r

$$\rho(T,P) = \rho_r (1 - \alpha(T - T_s) + K_T^{-1}(P - P_h)) \quad (7)$$

where T_s is the adiabatic temperature distribution and P_h is the hydrostatic pressure. The reference density can then be derived as the solution of the Adams Williamson equation

$$\frac{1}{\rho_r} \frac{\partial \rho_r}{\partial z} = -\frac{g \rho_r}{K_S} = -\frac{1}{h} \frac{Di}{\gamma} \quad (8)$$

z is the vertical coordinate pointing upward. Assuming Di and γ as constant in the convecting layer, equation (8) can be integrated:

$$\rho_r = \rho_o \exp((h-z)\, Di/\gamma) \quad (9)$$

with ρ_o being the density at the surface. In the following the equations are nondimensionalized

according to (primes denote nondimensional quantities)

$$(x,z) = (x',z')h \qquad \vec{v} = \vec{v}'\,\kappa_o/h$$

$$t = t'h^2/\kappa_o \qquad T = T'\Delta T \qquad (10)$$

$$H = H'c_p\Delta T\kappa_o/h^2 \qquad \eta = \eta'\eta_o$$

with κ_o being the thermal diffusivity at the surface ($\kappa = k/\rho c_p$) and ΔT being the temperature difference between top and bottom of the convecting layer; η_o is (1) the constant viscosity, (2) the surface viscosity in the Newtonian models, or (3) a scaling viscosity in the non-Newtonian models. In the following the primes are dropped. The equations are simplified as follows: Inertial forces are neglected (left-hand side of (4) is dropped). The anelastic liquid approximation is applied (time derivative in (3), pressure derivative in (5), and η_b term in (6) are neglected). The thermal conductivity k is assumed constant. The hydrostatic pressure P_h = $P-P_l$ (where P_l is the nonhydrostatic pressure) is eliminated by taking the curl of (4). The resulting system of equations in terms of the streamfunction ψ is then given by

$$2\frac{\partial^2}{\partial x\partial z}\,\eta e^{zDi/\gamma}\,\left(2\frac{\partial^2\psi}{\partial x\partial z} + \frac{Di}{\gamma}\frac{\partial\psi}{\partial x}\right)$$

$$+ \left(\frac{\partial^2}{\partial z^2} - \frac{\partial^2}{\partial x^2}\right)\eta e^{zDi/\gamma}\left(\frac{\partial^2\psi}{\partial z^2} - \frac{\partial^2\psi}{\partial x^2} + \frac{Di}{\gamma}\frac{\partial\psi}{\partial z}\right)$$

$$= Ra\,\rho_r\frac{\partial T}{\partial x} - \frac{Di}{\gamma}\frac{\partial P_1}{\partial x} \qquad (11)$$

$$\rho_r\left[\frac{\partial T}{\partial t} + (\vec{v}\nabla)T + Di(T+T_o)v_z\right] = \nabla^2 T$$

$$+ 2\,\frac{Di}{Ra}\,\eta(e^{*2}_{ij} + \frac{2}{3}(\nabla\vec{v})^2) + \rho_r H \qquad (12)$$

$$\vec{V} = e^{zDi/\gamma}\begin{bmatrix}\partial\psi/\partial z\\ -\partial\psi/\partial x\end{bmatrix} \qquad (13)$$

$$\rho_r = \exp[(1-z)Di/\gamma] \qquad (14)$$

$$e^{*}_{ij} = \frac{1}{2}\left(\frac{\partial v_i}{\partial x_j} + \frac{\partial v_j}{\partial x_i}\right) - \frac{1}{3}\nabla\vec{v} \qquad (15)$$

$$\vec{\nabla v} = v_z\,Di/\gamma \qquad (16)$$

$$Ra = \frac{\rho_o g\alpha\Delta T h^3}{\kappa_o\eta_o} \qquad (17)$$

Here e^*_{ij} is the deviatoric strain rate and Ra is the Rayleigh number. It can be seen that the thermal effect of compressibility enters through the terms containing Di alone (equation (12)), while the mechanical effect (i.e., the variation of ρ) enters through the terms with Di/γ (equations (11) and (13)-(16)).

It is convenient to define an effective Rayleigh number Ra* by

$$Ra^* = \frac{\bar{\rho} g\alpha\Delta T^* h^3}{\bar{\kappa}\eta_o} \qquad (18)$$

where the overbar denotes vertical means and ΔT^* is the overadiabatic temperature difference between top and bottom

$$\Delta T^* = \Delta T(1-Di(\bar{T}+T_o)/\Delta T) \qquad (19)$$

The vertical means

$$\bar{\rho} = \rho_o\,\frac{\gamma}{Di}(e^{Di/\gamma} - 1) \qquad (20)$$

$$\bar{\kappa} = \frac{k}{\rho_o c_p}\,\frac{\rho_o}{\bar{\rho}} \qquad (21)$$

can be inserted into (18). In case of Di/γ <1, (18) can be expanded into a Taylor series

$$Ra^* = Ra(1-Di(\bar{T}+T_o)/\Delta T)(1+\frac{1}{2}\,\frac{Di}{\gamma}+\ \ldots) \qquad (22)$$

We note that the adiabatic temperature gradient decreases Ra*, while compressibility (Di/γ) increases Ra*.

Equation (11) and (12) are solved by finite differences (FD) on an equidistant grid in a rectangular aspect ratio 1 box. The nonsymmetric system of the FD equations of (1) is solved by Gaussian elimination with partial pivoting. If Di/γ = 0, Cholesky decomposition of the symmetric matrix can be applied. The heat equation is solved by an ADI method in combination with Spalding's (1972) upwind scheme. For steady state solutions an underrelaxation technique was used (Christensen, 1984). The incompressible version of the code reproduced all cases of the convection benchmark test (Blankenbach et al., 1989). The compressible version was tested by a few cases of Jarvis and McKenzie (1980). Checking the energy balance of the models gave imbalances of less than 2-3% for the constant viscosity models with up to 61x61 grids (except for γ = 0.2, where the imbalance was 8%). In some of the models with variable viscosity the grid was relatively coarse (see Table 1) because of economic reasons. Resolution checks with grid spacings up to 61x61 have been carried out for some of the models marked by [a] (Table 1). The shapes of the flow, temperature, and viscosity fields are well resolved, and global parameters like the mean velocity or temperature are correct to within a few percent. The thermal boundary layers sometimes reached the resolution of the grid. Energy imbalances up to 20% and an underestimation of the Nusselt number by at most 10% were the consequence. The differences between the mean viscous heating and adiabatic heating and cooling, which globally should be balanced, were less than 2% for the Newtonian models and about 7% for the non-Newtonian models.

As top and bottom boundary conditions, free slip and constant temperature (T=0 at the top and 1 at the bottom in nondimensional units) were chosen. T_o was kept at 0.273 for all models. The side walls were reflective. Di is varied between 0 and 1 (0.58 in the constant viscosity models). In the constant viscosity models the Grüneisen parameter γ is varied between infinity (incompressible) and 0.2, while in the variable viscosity models, γ is chosen to be either infinite or 0.8. Taking possible thermodynamic values for the mantle (Stacey, 1977; Knittle et al., 1986), Di

TABLE 1. Summary of Models

Model Set	Rheology (Equation)	A	E, a	V	n	Ra	Di	γ	Approximation	Grid	Figure
1	const	-	-	-	-	10^5	0-0.58	∞-0.4	ALA	41x41	1
2	const	-	-	-	-	10^5	0-0.58	1.1	ALA tr.	41x41[a]	2
3	const	-	-	-	-	10^5	0.58	∞-0.2	ALA	41x41[a]	3
4	b	1	6.91	-	1	10^4	0-0.75	∞,0.8	EBA, ALA tr.	41x41[a]	4
5	c	10^{-8}	38.48	18.45	1	10^5	0-1.0	∞,0.8	EBA, ALA tr.	41x41[a]	5
6	c	$0.58x10^{-9}$	76.91	36.91	3	10^5	0-1.0	∞,0.8	EBA, ALA tr.	31x31[a]	6, 7
7	c	10^{-16}	76.91	36.91	1	10^5	0.1.0	∞,0.8	EBA, ALA tr.	51x51	8
8	c	$0.58x10^{-9}$	76.91	36.91	3	$2x10^5$[b]	0-1.0	∞,0.8	EBA, ALA tr.	41x41	9, 10

Rheology parameters are nondimensional. Approximations: ALA, anelastic liquid approximation; tr., truncated; EBA, extended Boussinesq approximation. Boundary conditions in all models: free slip on all sides, constant temperature at the bottom. T_o=0.273 in all models, Θ_o=2.09 in models 5-8.
[a] Resolution checks with grids up to 61x61 have been carried out.
[b] H=5.

lies between 0.3 and 1.0, while γ varies between 0.75 and 1.

Three different rheologies were chosen: (1) constant viscosity, (2) temperature dependent viscosity:

$$\eta = \exp(-aT) \tag{23}$$

(3) temperature-, pressure-, and stress-dependent viscosity:

$$\eta = A\,\tau_{II}^{1-n}\,\exp\frac{E + V(1-z)}{T + \Theta_o} \tag{24}$$

where τ_{II} is the second invariant of the viscous stress tensor, E and V are activation energy and volume, respectively, and Θ_o is a constant, which was chosen different from T_o for practical reasons (if Θ_o=T_o, then the upper part of the convective layer would become a stagnant lid).

Different approximations can be chosen when solving equations (11)-(16). For the case Di=0 the equations reduce to the Boussinesq approximation (with variable viscosity). The case Di=0, but Di/γ≠0 is referred to as the "extended Boussinesq approximation" (EBA). Only the thermal effect of compression is accounted for. For both Di≠0 and Di/γ≠0, the equations represent the "anelastic liquid approximation" (ALA). For γ not too small (γ>0.8), computation time is saved if the pressure induced buoyancy term on the right-hand side of equation (11) is neglected (ALA truncated). For a comparison of the different approximations with the mean field approach, the reader is referred to Quareni and Yuen (1988).

The geoid is calculated by the Fourier approach; that is, the deflections of the surface and bottom and the density variations due to temperature and pressure are approximated by thin horizontal mass sheets. The mass distribution on each sheet is decomposed into a Fourier series, whose components give directly the corresponding geoid contributions (see Marquart and Schmeling, (1989) for details).

3. Results

3.1. Constant Viscosity Convection

Figure 1 shows the flow and temperature fields of constant viscosity convection (model 1, see Table 1). Increasing Di and Di/γ from 0 (Figure 1a, Boussinesq approximation) to Di=0.58 and γ=1.1 (Figure 1b, ALA) essentially leads to the establishment of an adiabatic temperature gradient and a decrease in flow velocity. A decrease of γ (Figure 1c) leads to a slight concentration of the flow downward. This behavior stems from the dependence of the buoyancy term in the equation of motion (11) on the density increase with depth.

Figure 2 shows the effect of increasing Di (γ=1.1 in the ALA) on the horizontally averaged temperature (Figure 2a), the Nusselt number Nu, the mean flow velocity v_{RMS}, and the overall dissipation $\bar{\Phi}$ (Figure 2b), the topography (Figure 2c), and the geoid undulation (Figure 2d). For the determination of the dimensional topography and geoid the following parameters have been chosen: $h=10^6$ m, ΔT=1000K, $\eta_o=10^{22}$ Pa s, $\rho_o=4x10^3$ kg m^{-3}, $\alpha=2.5x10^{-5}$ K^{-1}, g=10 m s^{-2},

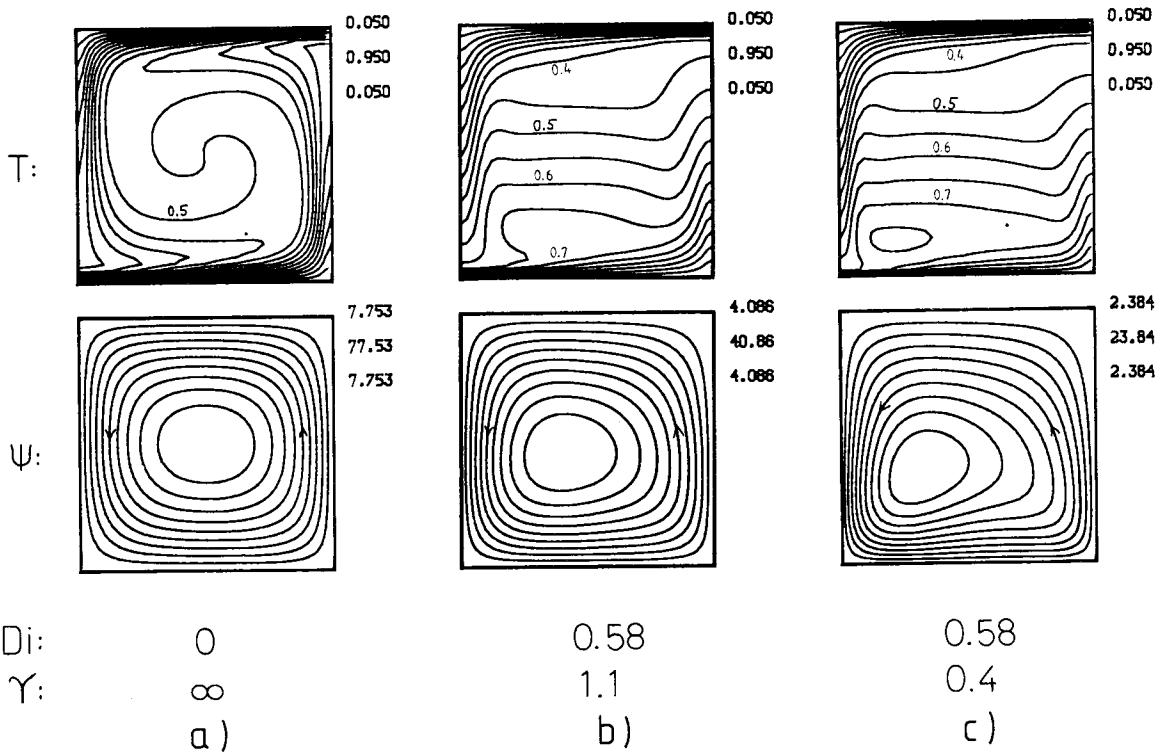

Fig. 1. Constant viscosity convection with $Ra=10^5$ and fixed temperature at the bottom (model set 1, see Table 1). Top row shows isotherms; bottom row shows streamlines. The lowest and highest values of the nondimensional temperature and stream function and their increments are given beside the boxes, respectively. (1) Dissipation number=0, i.e., Boussinesq approximation. (b) and (c) Fully compressible solutions (ALA) for Di=0.58 and γ=1.1 and 0.4, respectively. Note the establishment of an adiabatic temperature gradient and the asymmetry between the upwelling and downwelling flows in the compressible cases.

$\kappa_o=10^{-6}$ m^2 s^{-1}. We note that increasing Di decreases the overadiabatic temperature difference, i.e., Ra*, thereby decreasing the vigor of convection as well as topography and geoid. The bottom topography has a similar peak to peak amplitude as the top topography if a density contrast of $\Delta\rho=\rho_o$ is assumed at the bottom (not shown).

The effect of variation of γ for constant Di is shown in Figure 3. The extreme case of γ=0.2 implies an increase in density with depth by a factor of 18. Note that the mass flow near the bottom is accomplished by a much smaller velocity than in the less dense upper region. Decreasing γ increases Ra* and consequently Nu by a small amount (not shown) as well as $\bar{T}(z)$ (Figure 3b). An increase in $\bar{T}(z)$ with the adiabatic gradient remaining approximately constant leads to a decrease in the thickness of the lower thermal boundary layer. It is noteworthy, that the slight increase in convective vigor (or Nu) can take place with a decrease in the mean flow velocity (Figure 3a)! Figures 3c-3e show that even a strongly compressible mantle does not change the geoid undulation significantly. To understand this, Figure 3e shows the contributions from topography (N_{Topo}), temperature (N_{Temp}), and pressure induced density variations (N_{Press}) which lead (together with the deflection of the convective bottom, whose contribution is not shown) to the total geoid amplitude (N_{total}). An increasing N_{Press} is compensated by a decreasing N_{Topo}; thus any lateral density variation produced by compression is dynamically compensated by topography changes and does not lead to a significant geoid signal.

3.2. Variable Viscosity Models

A set of models has been calculated with purely temperature dependent viscosity according to (23) (model 4, see Table 1). For Di=0, this model was identical to the benchmark model 2a of Blankenbach et al. (1989). The effects of increasing Di on the temperature, viscosity, Nusselt number, mean velocity, and mean dissipation are shown in Figure 4. Since there is no pressure dependence in the viscosity, there develops a thick stagnant lid which keeps the temperature of the interior of the cell well above 0.5 (=mean between top and bottom) (Figure 4a, Di=0). The establishment of an adiabatic temperature gradient with increasing Di decreases the temperature within the most parts of the cell. As a consequence, $\eta(T)$ increases everywhere except near the bottom (Figure 4b). Both the increasing mean viscosity and the decreasing overadiabatic temperature difference (or Ra*) slows down the mean velocity v_{RMS} and Nu (Figure 4c). In contrast to the constant viscosity case, the bottom topography is smaller than the top topography by a factor of approximately 3 for

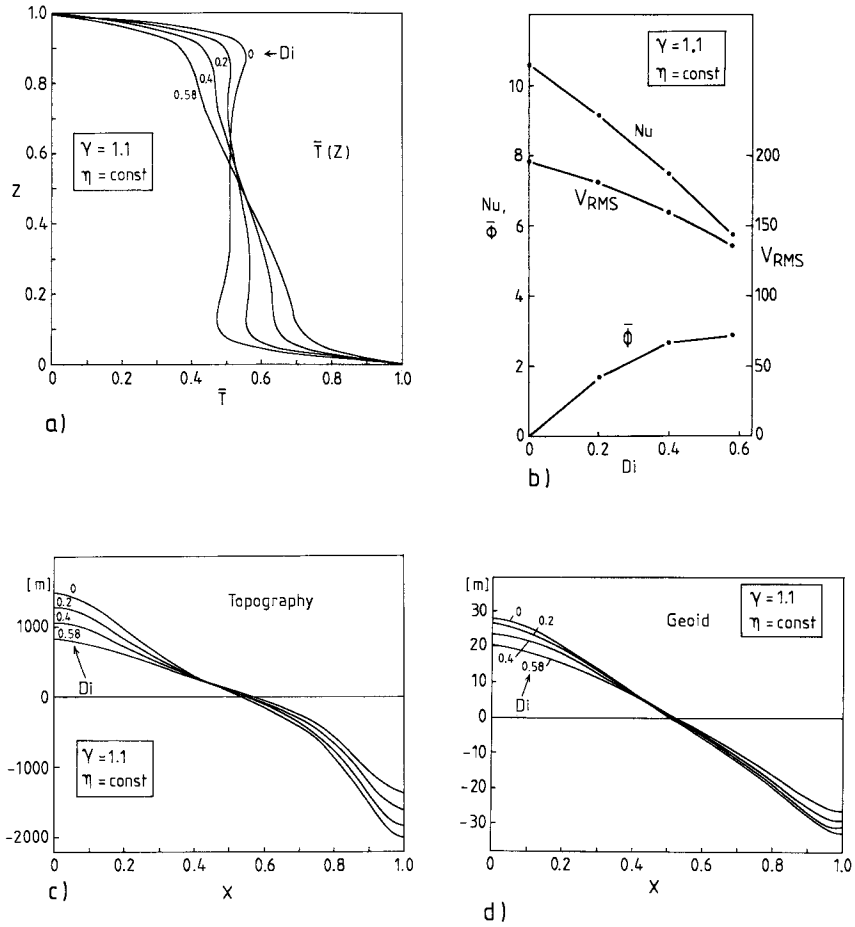

Fig. 2. Effect of varying Di in constant viscosity convection with $Ra=10^5$, $\gamma=1.1$, and fixed bottom temperature (model set 2). The ALA was used. (a) Vertical temperature profiles (horizontally averaged). (b) Nusselt number Nu, root mean square average velocity v_{RMS}, and mean viscous dissipation $\bar{\phi}$ as functions of Di. All in nondimensional units. (c) and (d) Surface topography and geoid undulation profiles. The upwelling is on the left side. Note that increasing Di generally decreases convective vigor.

Di=0. A further decrease of the viscosity near the bottom at higher Di reduces the bottom topography even more to less than 500 m peak to peak amplitude if scaled in the same way as the constant viscosity models (not shown).

In the next model set (number 5, see Table 1), a rheology law according to equation (24) is chosen, assuming Newtonian behavior (n=1) (see also Christensen, 1984). The unrealistic high value of $\Theta_o=2.09$ is taken to avoid extremely high viscosities near the surface, i.e., to mimic weakening processes near the surface which aid spreading and subduction. By this assumption and due to the pressure dependence of the viscosity the flow now becomes concentrated near the surface. The flow lines, temperature, and viscosity of model 5 are shown in Figure 5 for different dissipation numbers. Steady state solutions are obtained for Di values up to 0.75, oscillatory behavior is observed for Di=1 using the extended Boussinesq approximation (EBA), while the flow becomes chaotic for Di=1 in the truncated anelastic liquid approximation (ALA) (see the flow at different arbitrarily taken times t_1 and t_2 in Figure 5). In contrast to the previous model 4, increasing Di increases the mean cell temperature, thereby decreases the mean viscosity and increases the convective vigor. For high Di the flow tries to fill the whole box, the downwelling flow region narrows and the upwelling plume becomes weaker.

Figure 6 shows the next set of models assuming a non-Newtonian (n=3) rheology (see Table 1, model 6). According to Christensen's (1983) empirical law, the activation energy and volume are chosen to be twice as high as in the previous model to obtain a similar flow field (for Di=0). Steady state solutions of the EBA for Di increasing from 0 to 1 and an ALA-truncated solution for Di=1 and $\gamma=0.8$ are shown. The main effect of increasing Di and Di/γ is a concentration of the downwelling flow (i.e., the formation of a "slab") and a broadening of the upwelling flow. (This occurred also in the previous Newtonian models, but to a lesser extent.) This behavior is partly caused by the upwarpings of the isotherms near the downwelling limb and partly by the strain rate softening effect of the power law rheology. Both effects locally reduce the viscosity and decouple the cold descending flow from the center of the cell. The decoupling zone is dashed for the case Di=1 (Figure 6). It

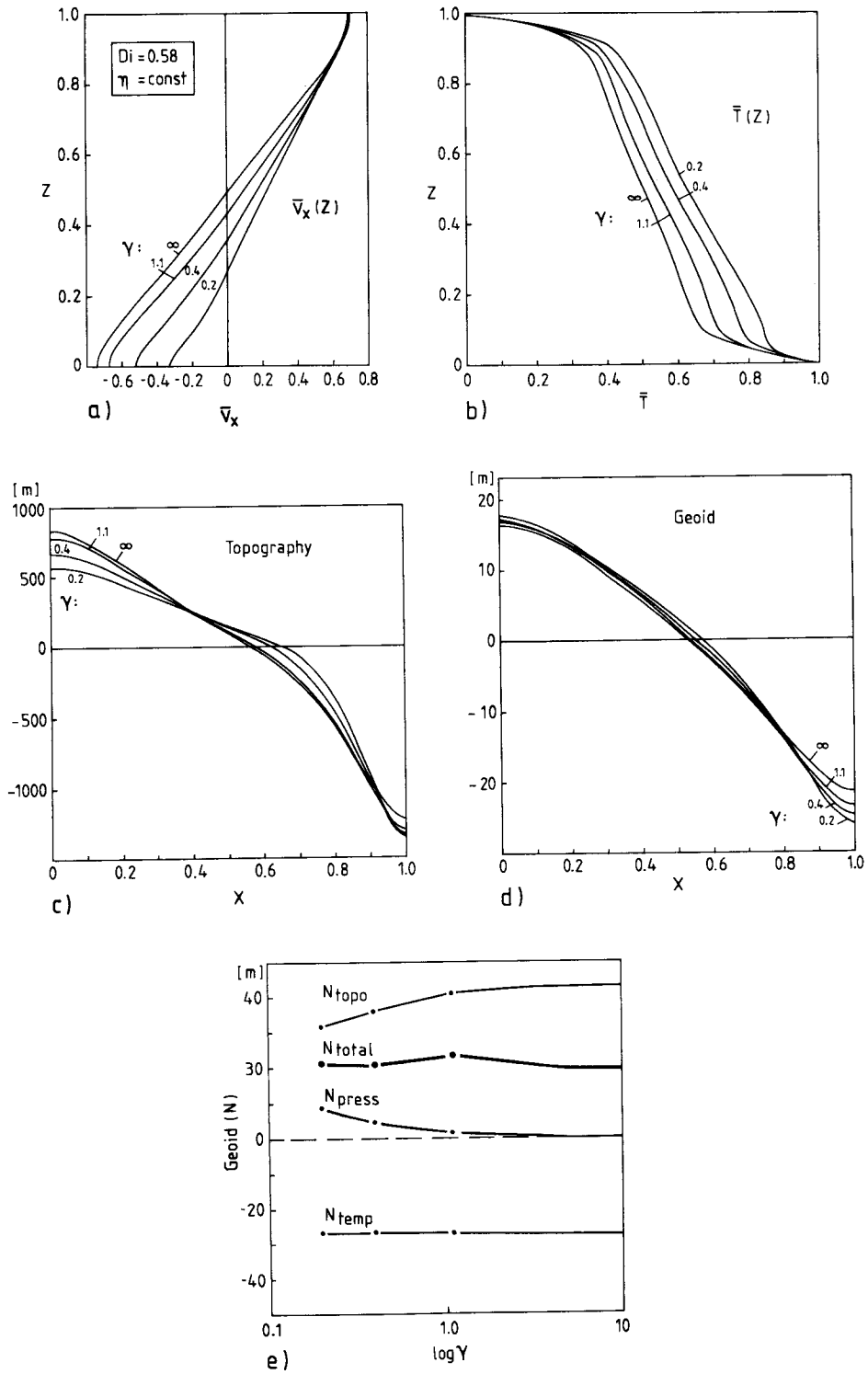

Fig. 3. Effect of varying the compressibility or γ in constant viscosity convection, $Ra=10^5$, Di=0.58 (model set 3). (a) Horizontal velocity as a function of depth (horizontally averaged and normalized by the maximum vertical velocity, which lies between 288 and 393). (b) Temperature profiles (horizontally averaged, nondimensional). Note the increase in mean temperature and the decrease in the thickness of the lower thermal boundary layer with increasing compressibility. (c) and (d) Surface topography and geoid undulations above the convection cell. The geoid is virtually independent of the compressibility despite density variations as high as by a factor of 18! (e) Single contributions to the total geoid, produced by pressure- and temperature-induced density variations and topography. Total amplitudes are shown. Note that variations in N_{Topo} and N_{Press} cancel, leaving N_{total} constant.

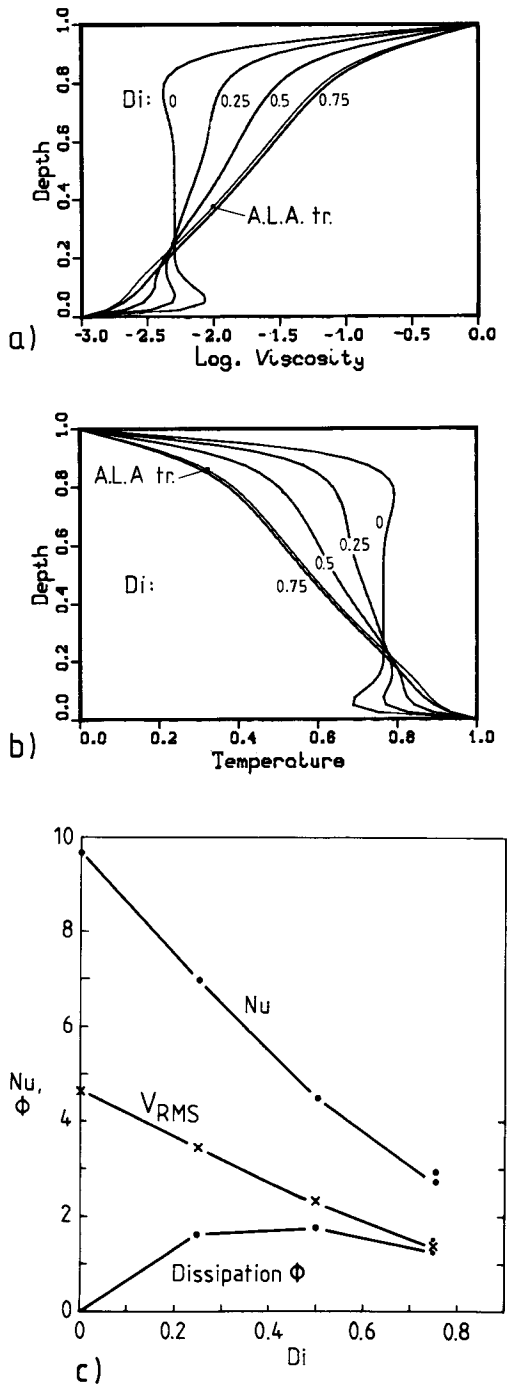

Fig. 4. Results for convection models (model set 4) with temperature-dependent viscosity for different dissipation numbers Di. The Grüneisen parameter was fixed at 0.8. (a) Nondimensional temperature profiles, horizontally averaged. The EBA was used for all Di values. In addition, the truncated ALA was used for Di=0.75. Note the decreasing mean temperature as Di is increased. (b) Logarithmic nondimensional viscosity profiles, horizontally averaged. Again, the Di=0.75 case was repeated using the truncated ALA, else the EBA was used. (c) The Nusselt number, mean nondimensional velocity, and dissipation as functions of Di. Note the decrease in convective vigor as Di increases.

is this viscosity contrast between the highly viscous descending flow and its soft surrounding, which leads to the "slab"-like behavior of the downwelling region. The soft decoupling zone extends to the upper right corner, where beside efficient strain rate softening, the viscosity is also reduced by strong viscous dissipation. See also section 4 for a further discussion of this nonlinear coupling between variable viscosity and adiabatic and viscous heating.

Another interesting feature is the difference between the EBA and the ALA with γ=0.8. The flow geometry changes significantly if vertical density variations are accounted for in the equation of motion (4 or 11) which is proportional to ρ_r, while the viscous forces are independent of ρ (equation (6)). Thus the lower part of the "slab" of the ALA case (Figure 6) has a stronger negative buoyancy than it has in the EBA case. As a result, the ALA concentrates the downwelling flow even more; the maximum vertical velocity increases from 670 (EBA) to about 1000 (ALA) in nondimensional units.

Another remarkable effect is shown in Figure 7 (and did, in fact, already occur in model 5, Figure 5). For incompressible convection the cell temperature is as low as 0.2 and increases as adiabatic heating is included. The opposite behavior was observed for model 4 (Figure 4), in which the mean cell temperature was above 0.5 as a consequence of a stagnant lid. As shown in Figure 7b, an increasing cell temperature decreases the cell viscosity. The vigor of convection first increases with increasing Di, followed by a decrease for very high Di-values (Figure 6c) as the overadiabatic temperature difference approaches 0.

Topography and geoid undulations could not be evaluated because the resolution of the grid needed for integration of the pressure field was insufficient.

To see if the development of a decoupling zone is a consequence of the high activation energy of model 6, a model with the same activation energy and volume but Newtonian rheology was calculated (model 7, Figure 8). A considerable narrowing of the descending plume is observed, which is, however, not as strong as in model 6. Furthermore, the low-viscosity decoupling zone bounding the descending flow ("slab") in the non-Newtonian model is missing in the Newtonian case.

In the following set of models, internal heating was considered so as to keep the bottom temperature constant. A nondimensional value of H=5 was chosen, corresponding to a potassium-depleted chondritic mantle with a radioactive heat generation of 3×10^{-12} W/kg. According to the nondimensionalization (10), the nondimensional H is identical to the quotient Ra_I/Ra with Ra_I =Rayleigh number based on internal heating (see, e.g., Machetel and Yuen, submitted manuscript, 1988).

Figure 9 shows the effect of increasing Di in the EBA. For Di=0 approximately half of the total surface flow is provided by bottom heating, which leads to a fairly narrow rising plume. For higher Di the cell temperature increases, reducing the viscosity but also the heat influx from the bottom. For Di=0.75, only 5% of the total heat flux is entering through the bottom; the rising plume is completely dispersed. Concentration of

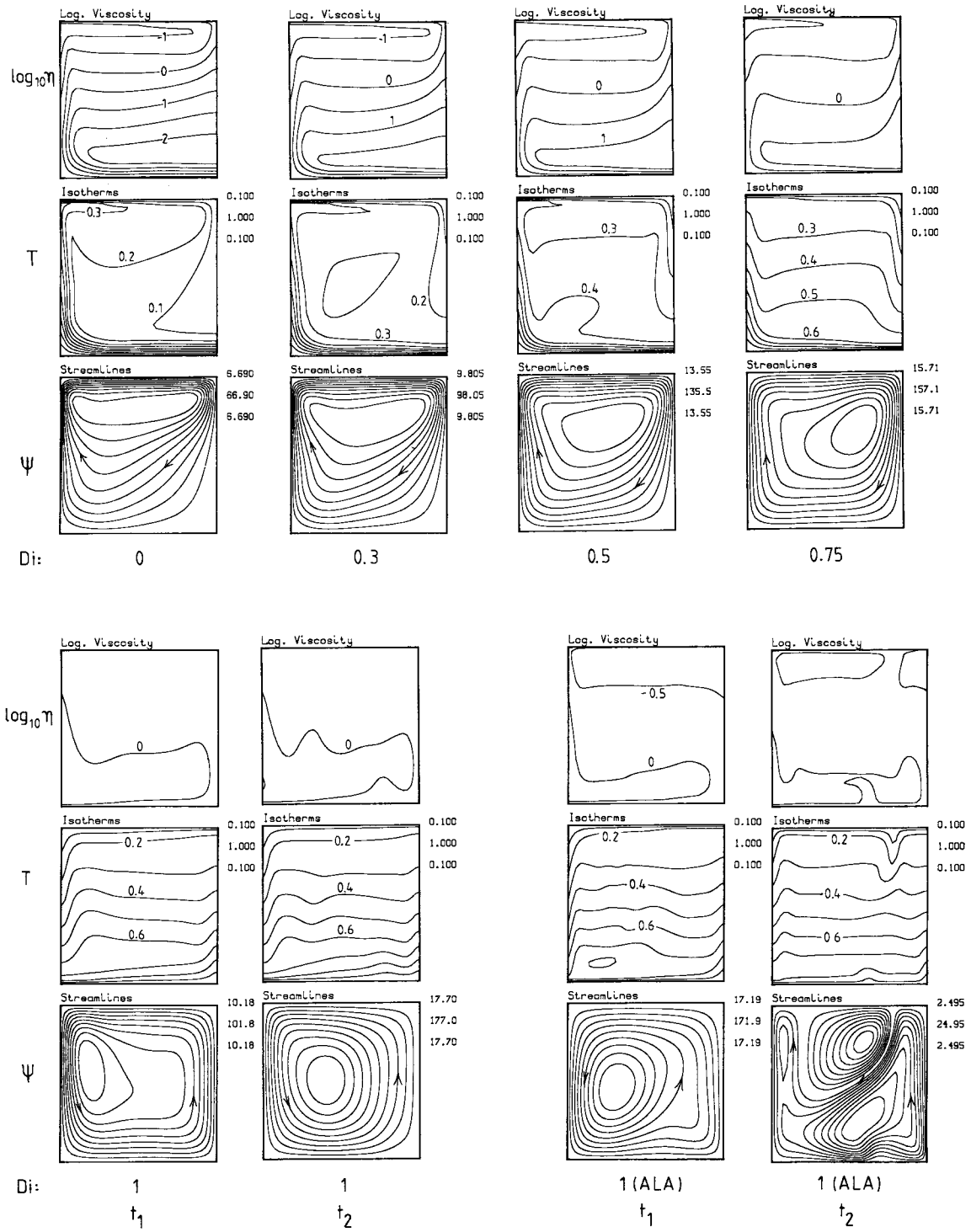

Fig. 5. Convection with a temperature- and pressure-dependent rheology (model set 5). Steady state solutions are shown in the top part of the Figure, where the dissipation number is varied from 0 to 0.75 toward the right. The EBA is used. For Di=1 time-dependent solutions were found (lower part of the figure, where also the flow directions are reversed). Two arbitrary stages are shown using the EBA (t_1 and t_2 on the left) and using the truncated ALA (t_1 and t_2 on the right). The EBA-solution shows oscillatory behavior, the truncated ALA-solution shows chaotic behavior. The Grüneisen-parameter was 0.8 in this case. (Top) Contour lines of the logarithmic, nondimensional viscosity fields. Note the change from a strong vertical stratification to a more evenly distributed viscosity field. (Center) Temperature fields. (Bottom) Streamlines. The lowest, highest, and incremental value of the nondimensional stream function is given near the upper right corner of each box.

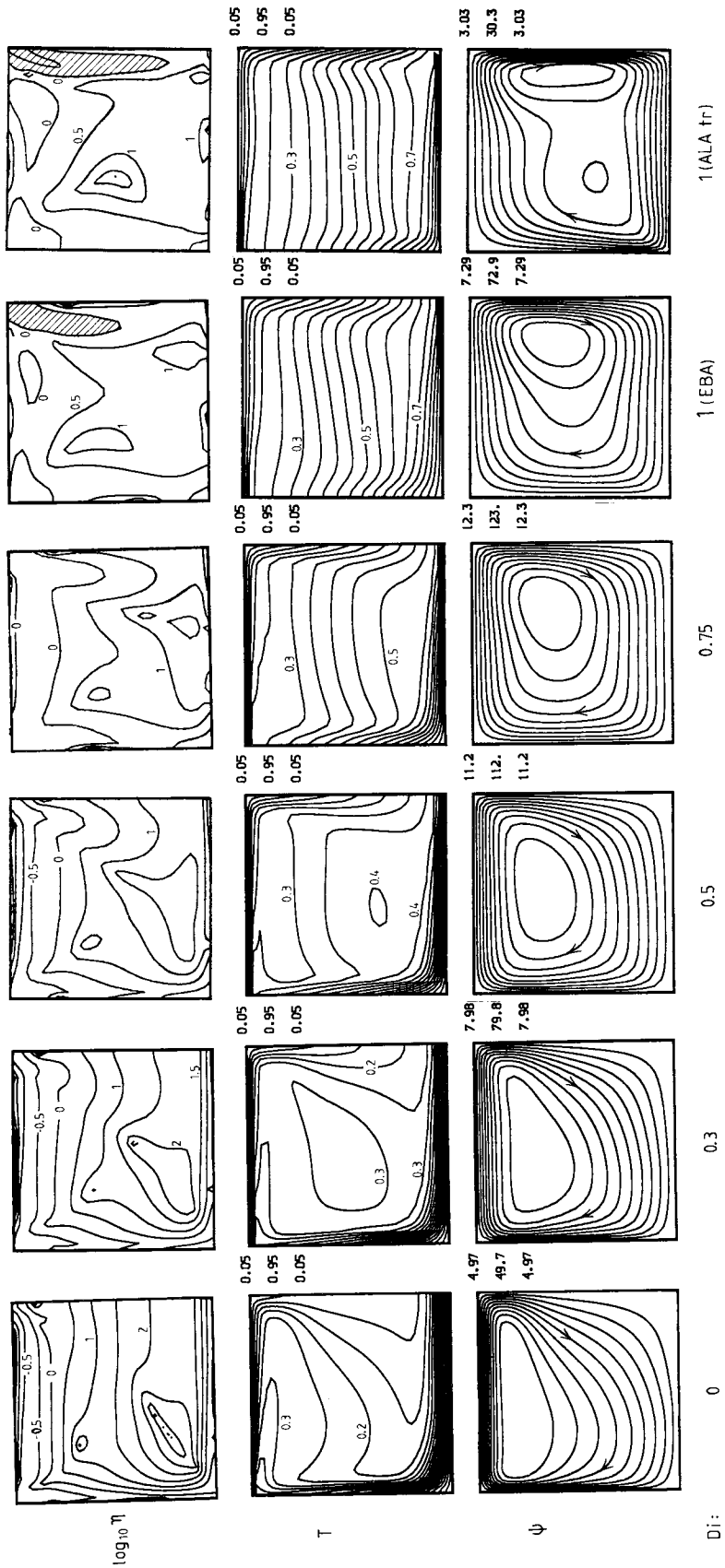

Fig. 6. Convection with a temperature-, pressure-, and stress-dependent rheology (model set 6). The activation enthalpy is twice that of model 5 (Figure 5). Note the resemblance with the model set 5 for Di=0. The dissipation number is varied from 0 to 1 toward the right. The EBA is used; in addition, the Di=1 case was repeated with the truncated ALA with a Grüneisen parameter of 0.8. (Top) Contour lines of the logarithmic, nondimensional viscosity field. Note the change from a strong vertical stratification to a more evenly distributed viscosity field and the formation of a soft decoupling zone (dashed) near the right wall as Di increases. It promotes the formation of a subducting "slab" for high Di values. (Center) Temperature field. (Bottom) Stream lines.

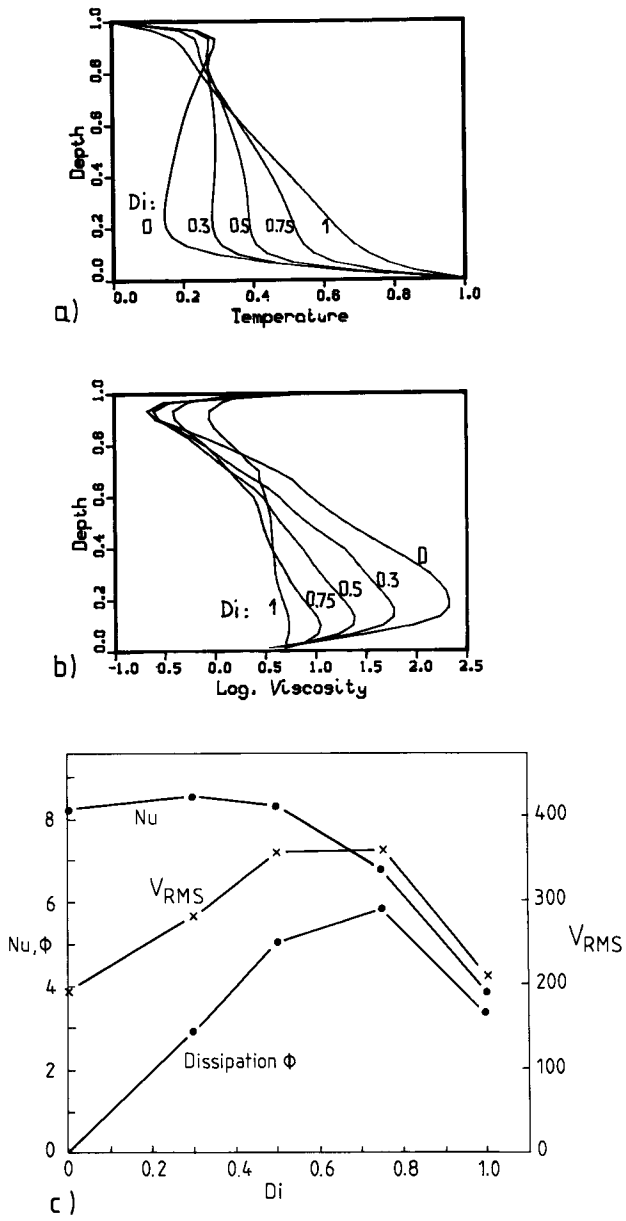

Fig. 7. (a) Temperature, (b) logarithmic viscosity, and (c) Nu, v_{RMS}, and dissipation for temperature-, pressure-, and stress-dependent rheology convection (model set 6). Otherwise like Figure 4. Note that the convective vigor is first increasing with Di in contrast to the model 4 (Figure 4).

the downwelling flow, which is a common feature of internally heated convection, is enhanced due to the nonlinear coupling between the temperature dependent rheology and adiabatic and viscous heating as described above.

For Di=0.75 a model was calculated with a finite γ=0.8 using the truncated ALA and taking the EBA solution for Di=0.75 (Figure 9) as initial condition. It was not possible to obtain a steady state solution even with a strong underrelaxation. The cell broke up into two cells (Figure 10, t_1). Continuing with a time-dependent calculation showed a periodic behavior. The root mean square velocity v_{RMS} is shown in Figure 11 for a few cycles, the stages t_2 and t_3 of Figure 10 represent instances of minimum and maximum v_{RMS}. At t_2 dense blobs of material are forming at both edges of the box, which sink with maximum velocity at instance t_3. The time-dependent behavior can be described as an episodic release of cold material from the upper boundary. The vigor of such an event is aided by two nonlinear effects: (1) the viscous decoupling of cold sinking material from the mantle (see above) and (2) the power law rheology, which reduces the overall viscosity by more than half a magnitude (compare the viscosity fields at t_2 and t_3).

It should be noted that the total internal heat production in the ALA case was 60% larger compared to the EBA case, since the mean density was higher by the same amount. A ALA run with H=3.02 was carried out which yields the same total heat production as the EBA case with H=5. No steady state solution could be found, suggesting that this case also shows time-dependent behavior.

4. Discussion

In this section the physical effects introduced by adiabatic and viscous heating and an increasing compression with depth will be discussed with emphasis on the nonlinear coupling with a variable viscosity.

4.1. "Slab" Formation by Nonlinear Coupling Between Compression and Rheology

Any vertical flow component lead to adiabatic heating or cooling. This produces an adiabatic temperature gradient which is given in nondimensional form as

$$\left(\frac{\partial T}{\partial z}\right)_s = Di(T+T_o) \qquad (25)$$

The dependence of the adiabatic gradient on temperature has important consequences for variable viscosity convection. The temperature field of incompressible, high Rayleigh number convection can usually be divided into three regions: (1) an isothermal core of the cell, (2) cold and hot thermal boundary layers with their corresponding vertical plumes, and (3) overshoot temperature layers adjacent to the regions of 2 (Figure 12b). These overshoot regions, which are advected remnants of the vertical plumes, are broadening due to thermal diffusion (see, e.g., the incompressible model in Figure 1 or the horizontal temperature profiles across the convection cells of Jarvis and Peltier (1988)).

In the case of adiabatic heating, the differences in temperature of the vertically moving regions 1, 2, 3 (Figure 12b) lead to different vertical adiabatic temperature gradients according to (25). In particular, in a downwelling overshoot region 3 the adiabatic temperature gradient is highest (Figure 12a); thus the adiabatic heating counteracts the lateral diffusion, thereby prolonging the lifetime of region 3. In contrast, adiabatic cooling in the upwelling flow leads to temperature profiles in regions 1, 2, and 3 approaching each other (Figure 12c).

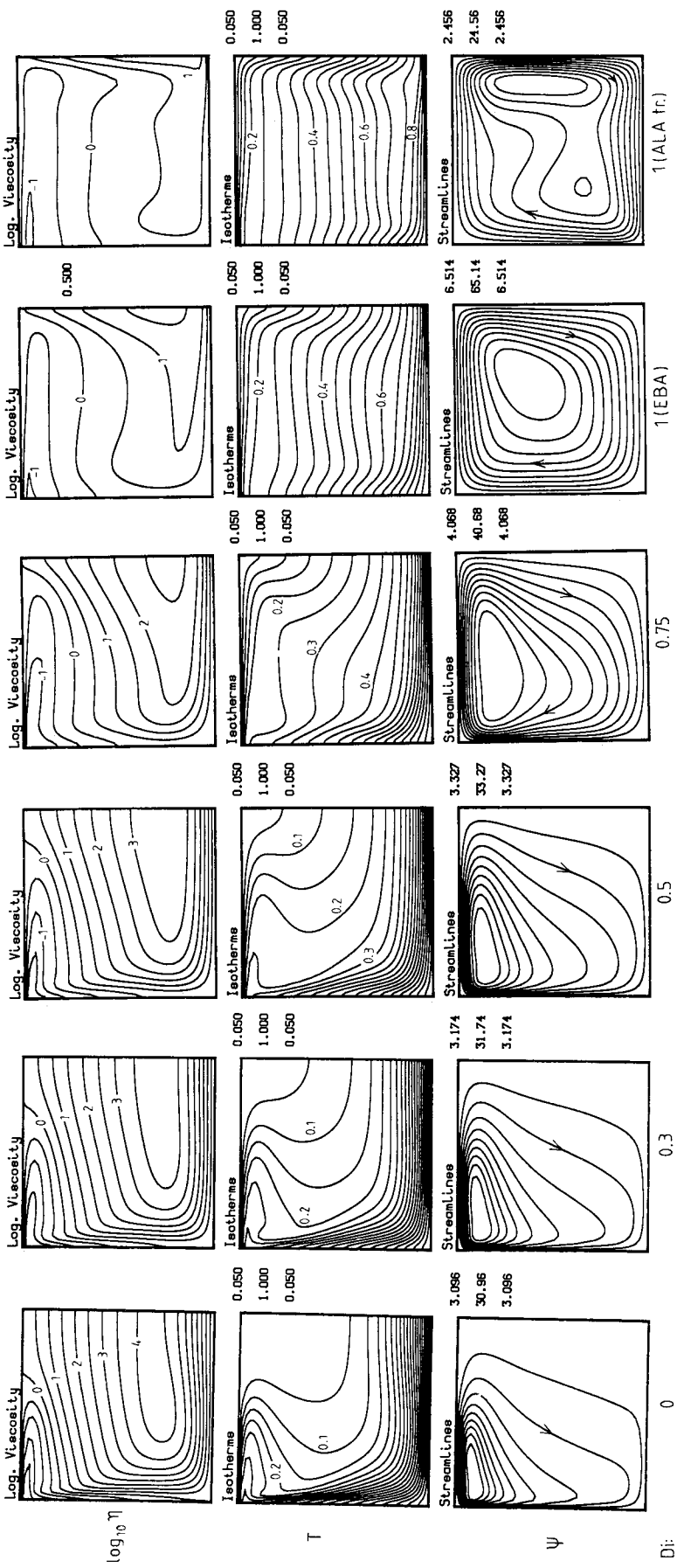

Fig. 8. Model set 7 which has the same activation enthalpy as model 6 (Figure 6) but a Newtonian rheology. The dissipation number is varied from 0 to 1 toward the right. The EBA is used; in addition, the Di=1 case was repeated with the truncated ALA with a Grüneisen parameter of 0.8. Note that the viscosity field (top row) does not show the development of a vertical low viscous decoupling zone as in the non-Newtonian case. Also, the concentration of the downwelling flow is much less pronounced (see streamlines in the bottom row).

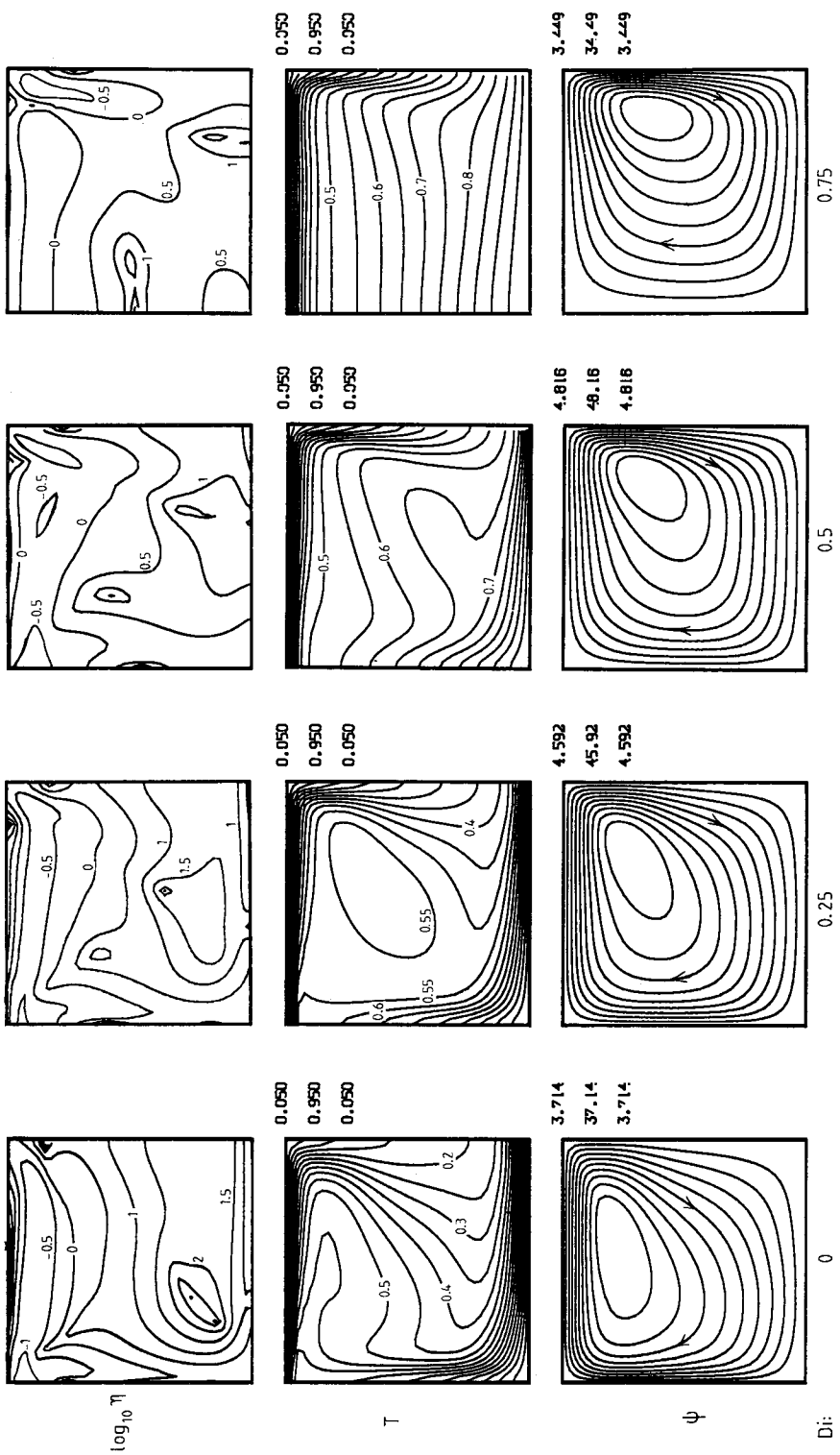

Fig. 9. Convection with internal heating (H=5) and a fixed bottom temperature (model set 8). The Rayleigh number is 1/5 of that in Figure 6; other parameters and the rheology are the same. The EBA is used throughout. Steady state solutions could be obtained.

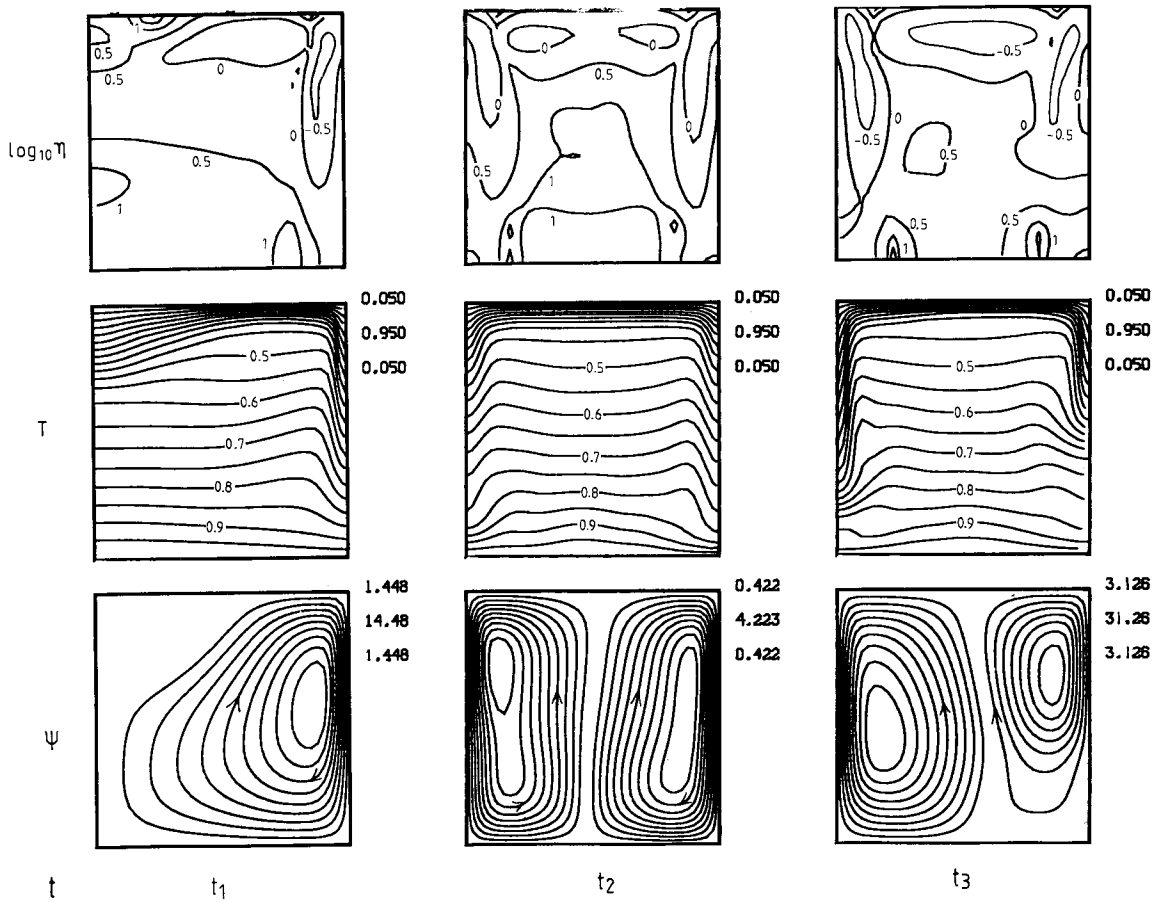

Fig. 10. Convection with internal heating (H=5), fixed bottom temperature, and Di=0.75 (model set 8). In contrast to the model in Figure 9, the truncated ALA is used resulting in time-dependent behavior. The Di=0.75 model of Figure 9 was taken as initial condition. The cell split up (t_1) into two cells which showed oscillatory behavior. The stages t_2 and t_3 represent instances of minimum and maximum root mean square velocity. Note the two cold plumes of different penetration depths at the instance t_3.

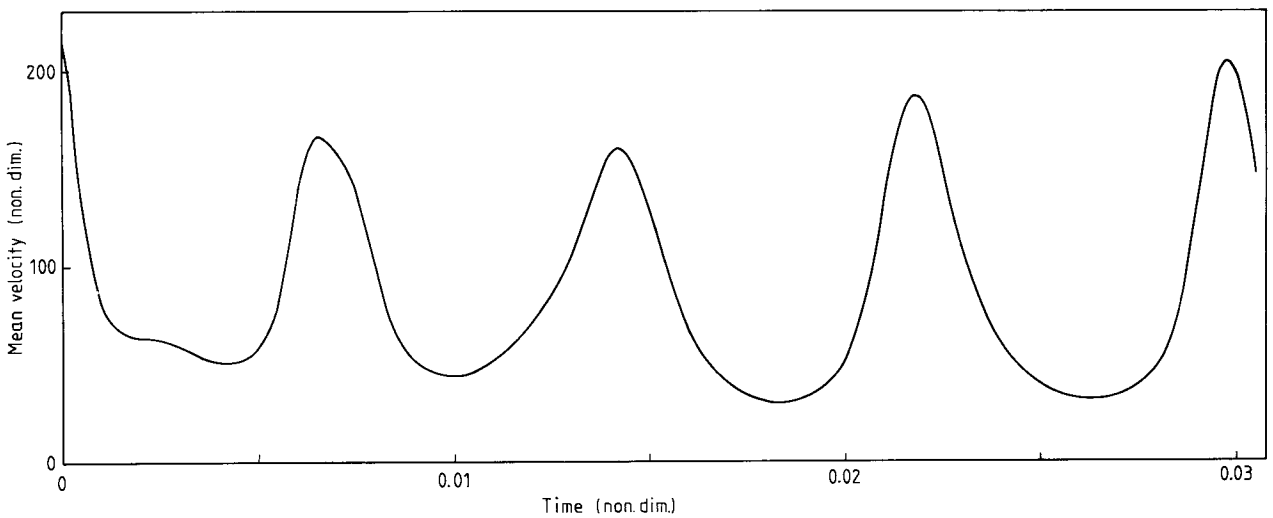

Fig. 11. Root mean square velocity (nondimensional) versus nondimensional time of the internally heated model 8 shown in Figure 10.

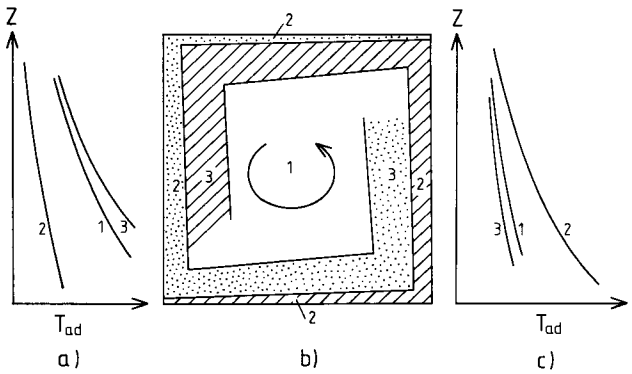

Fig. 12. Sketch of the three thermal regimes in high Rayleigh number convection heated from below, together with their adiabatic temperature distributions (qualitatively). (a) Adiabatic temperatures in the downwelling regions 1, 2, 3. (b) Region 1, adiabatic cell core; 2, horizontal boundary layers and corresponding vertical plumes; 3, temperature overshoot regions, which are remnants of regions 2. (c) Adiabatic temperatures in the upwelling regions 1, 2, 3. Note that the temperature profiles in the downwelling region diverge during descent, while the profiles in the upwelling region converge during ascent. This is a consequence of different adiabatic temperature gradients, which depend on the absolute temperature.

These differences between upwelling and downwelling flows lead to a concentration of buoyancy forces toward the downwelling region and thus a narrowing of that part of the flow. Furthermore, an increasing temperature difference with depth between the downwelling plume and adjacent fluid leads to still significant or even increasing buoyancy forces at the lower part of the downwelling region despite of lateral diffusion of heat. This effect could counteract the dispersal of subducted slabs in the mantle.

The above mechanism is dramatically enhanced if the viscosity is temperature- and stress-dependent: Due to the increasing temperature (and thus viscosity) difference the downgoing flow becomes mechanically decoupled from the overshoot region 3 and resembles a stiff slab (cf. Figures 6, 9, and 10). A non-Newtonian rheology strongly enhances this effect (cf. Figures 6 and 8). On the other hand, narrow upwelling plumes, which are often regarded as a consequence of a strongly temperature dependent viscosity (e.g., Loper and Stacey, 1983), are broadened by the decrease of lateral temperature (and viscosity) variations.

In addition to adiabatic and viscous heating a vertically increasing density has several important effects (cf. equations (11) and (12)):

1. The thermal buoyancy term in (11) is proportional to ρ_r; thus the convective driving forces increase with depth.
2. Keeping k_o constant, $\kappa(=k_o/\rho\, c_p)$ decreases with depth.

Both effects concentrate the flow downward, which is clearly seen in all models with ALA. It should, however, be noted, that additional effects, not accounted for in this study, might work in the opposite direction. In particular, a thermal expansivity α decreasing with ρ and a thermal conductivity k increasing with ρ (Anderson, 1987) would decrease buoyancy forces with depth.

The downward concentration of the flow and the higher density near the bottom as investigated in this study have some more important consequences.

4.2. Bottom Topography

The bottom topography increases with increasing compressibility (decreasing γ). For example, decreasing γ from 1.1 to 0.4 in the constant viscosity models increases the bottom topography by about 50% (Di=0.58). A similar increase was observed in the $\eta(T)$ models if γ is decreased from ∞ to 0.8 (Di=0.75). Similar increases of core-mantle boundary distortions were observed in the mean field solutions of Zhang and Yuen (1987), who also showed that such undulations decrease with increasing Ra. For the case of a depth-dependent α and k (with Di=0.6, γ=1.25) Zhang and Yuen (1988) found a decrease in the amplitude of the core-mantle boundary topography between 30 and 80% compared to constant α and k models. However, at least a part of this decrease would be compensated if γ would range between 0.75 and 1 as suggested by Stacey (1977).

4.3. Thermal Boundary Layer and Cell Temperature

The relative increase of the vigor in the lower part of the convective cell at decreasing γ values leads to a thinning of the lower thermal boundary layer (TBL) and, consequently, to an increase of the mean cell temperature (see Figure 3b). From the models discussed in section 3 one can estimate that the TBL thins by about 20 to 50% if γ is decreased from infinity to about 0.8. A relatively thin lower TBL is required if low seismic velocities in the lowermost 50-100 km of the mantle are interpreted as resulting from an increase in temperature (Doornbos and Mondt, 1979; Doornbos, 1983). The narrowing of the TBL thickness h_{th} can be accomplished by an increase in horizontal mass flow along the bottom of the cell due to an increase in convective vigor. This follows from the proportionality $h_{th} \sim \sqrt{\kappa/v_x}$, which gives, together with $\kappa \sim 1/\rho$

$$h_{th} \sim (\rho_r v_x)^{-\frac{1}{2}} \qquad (26)$$

Thus even though the flow velocities might be slower in the lower mantle than in the upper mantle (see, e.g., Figure 3a), they still can produce a thin TBL.

The increase in cell temperature is thus a consequence of the thinning of the lower TBL due to an increase of horizontal mass flow, or downward migration of the relative vigor of convective flow, keeping the temperature gradient constant. This is an alternative explanation to that of Yuen et al. (1987) and Quareni and Yuen (1988), who attributed the increase in temperature to an increase in shear heating due to viscous bulk compression (i.e., the term 4/3 Di $(\vec{\nabla}\vec{v})^2$/Ra η in equation (12)).

4.4. Independence of the Geoid on Compression

In the constant viscosity convection models it was found that lateral density variations induced by compression lead to geoid contributions (N_{Press} and a change in N_{Topo}, see Figure 3e) which nearly cancel out. This is a consequence of lateral density variations having their maximum amplitude near the upper and lower surfaces. They cause deflections of these surfaces, which result in local compensation of the gravity or geoid signal. This local compensation is a consequence of the gravity and geoid kernels approaching zero near the top and bottom of convection cells (Parsons and Daly, 1983; Ricard et al., 1984). Any mechanism shifting lateral pressure variations toward the midplane of the cell would lead to an enhanced geoid signal due to such variations. However, since such mechanisms (like viscosity stratification) would alter the stress and temperature fields by a larger amount, it can be concluded that the effect of compressible density changes on the geoid can be neglected in most cases.

4.5. Applicability to the Earth

First, the dimensionless quantities characteristic for convection in the Earth's mantle will be discussed briefly. Then the nondimensional model results will be scaled and extrapolated to the Earth.

The physical properties and quantities controlling mantle convection can be summarized as follows (see, e.g., Bott, 1982; Stacey, 1977; Knittle et al., 1986; Anderson, 1987; Hager and Gurnis, 1987; Ranalli, 1987; Williams et al., 1987; Heinz and Jeanloz, 1987): h=2900 km, ρ=3300-5500 (4000) kg/m^3, α=1-4x10^{-5} (2.5x10^{-5})K^{-1}, c_p=1250 J/K kg, g=10 m/s^2, κ=10^{-6} -2.5x10^{-6} (1.5x10^{-6}) m^2/s, ΔT=3000-4000 (3500) K, and η=10^{21}-10^{23} (10^{22}) Pa s. Preferred values used in this discussion are given in parentheses. The most uncertain quantity is the viscosity, which might also show the greatest variation with depth. The high viscosity estimates have been suggested to represent the lower mantle (Hager, 1984; Hager and Gurnis, 1987), while the upper mantle might have (at least regionally) a low-viscosity asthenosphere with viscosities even less than the minimum value given above.

Inserting the numbers given above into Di gives a range of Di from 0.3 to almost 1 with a preferred value of 0.58. From equation (19) the overadiabatic temperature difference ΔT^* can now be estimated to be roughly equal to the total ΔT minus approximately 1000K. Casting the above values into the Rayleigh number (18), the effective Ra of the mantle is expected to lie between 10^5 and 10^8, with 4x10^6 being the preferred estimate. Of course, this is only an order of magnitude estimate since the definition of a truely effective Rayleigh number with variable viscosity is complicated (Christensen, 1984), prohibiting an exact determination of Ra of the mantle.

The Nusselt number was defined as the ratio of the surface heat flow to k ΔT/h, k being the thermal conductivity (=κ ρ c_p). Taking an average surface heat flow of the Earth of 80 mW/m^2 (Sclater et al., 1981), the above values result in a Nusselt number between 3 and 20, with a typical value near 9. The surface velocities of the lithospheric plates are of the order of 3 cm/yr, or 1800 in nondimensional units, if scaled by equation (10) and the above preferred values.

Since virtually nothing is known about the rheological law and particularly its temperature dependence in the deep mantle, one might tentatively consider the well-studied olivine rheology. Assuming an activation energy of about 5.6x10^5 J/mol and an activation volume of 1.7x10^{-5} m^3/mol (Kirby, 1983), the viscosity will change by one order of magnitude if the temperature is changing by only 60K at midmantle levels.

The rheologies and Rayleigh numbers of the models have been chosen in a way that still steady state (or at most oscillatory) solutions could be obtained. The Rayleigh number of the constant viscosity models (models 1-3) are clearly too low compared to the Earth. If Ra is increased (e.g., by decreasing the viscosity), the topography and geoid undulations for the incompressible case will decrease proportionally to Ra$^{-0.18}$ and Ra$^{-0.31}$, respectively. These proportionalities follow from the models of Blankenbach et al. (1989). The main result of the constant viscosity models in this study, namely, the independence of the geoid on compression, can thus safely be extrapolated to higher Rayleigh numbers.

The Rayleigh numbers used to scale the variable viscosity models 4-8 (Table 1) imply scaling viscosities as high as 5.7x10^{24} Pa s (model 4) and 5.7x10^{22} Pa s (models 5-8). These viscosities have to be used for dimensionalization of the nondimensional viscosities in Figures 4-10. Inspecting these figures, typical model viscosities range between 10^{22} and 10^{24} Pa s. Averaging the viscosity by weighing it with the square of the strain rate (Parmentier et al., 1976), effective Rayleigh numbers could be calculated, which range about 10^6 ($\pm$ a factor of 2) for all models shown. These effective Rayleigh numbers, together with Nusselt numbers ranging about 8, and subducting velocities of about 1 cm/yr (e.g., obtained in model 5 for Di>0) show that the vigor of the convective models is only slightly less than that expected in the Earth mantle. However, even in the case of a much higher effective Rayleigh number, the promotion of slab formation, as found in this study, will persist: the overshoot (i.e., the decoupling) regions will be thinner, while the overshoot temperatures do not change significantly (see, e.g., the horizontal temperature profiles by Peltier (1980) or the overshoot temperatures of the models of Blankenbach et al. (1989)).

The temperature dependence of the rheology of the models had to be assumed to be considerably weaker than that of olivine because of numerical constraints. For instance, in model 5 a change in viscosity by one order of magnitude can be accomplished by a temperature change of 0.16 (nondimensional), i.e., 500K. (Note that a direct comparison of the activation energy used in the models with that of olivine is not reasonable because of the artificially high value of θ_o, see section 3.2 for a discussion of this choice.) Thus, in nature a much smaller horizontal change in temperature is sufficient to form a decoupling low-viscosity zone adjacent to the slab. With the same argument it can be anticipated, that this

decoupling will already take place for smaller dissipation numbers than in this study (possibly about 0.5). The decoupling zone also might extend to deeper levels than observed here. The argument is as follows: Any lateral temperature difference near the surface, δT_{top}, is amplified during adiabatic descent to the value $\delta T_{top} \exp(Di\ z)$, neglecting lateral diffusion (z is nondimensional depth). Lateral diffusion is proportional to the absolute value of δT. If the natural temperature dependence of the rheology is significantly stronger than assumed in this study, then a smaller lateral T difference is sufficient to form a decoupling zone. Lateral diffusion and dispersion will become less effective and the (smaller, but more effective) temperature difference will survive and may even increase down to greater depths.

With a stronger temperature dependence, a non-Newtonian rheology might not be necessary for the formation of the decoupling zone adjacent to the slab, contrary to the results of this study. However, such rheology might strongly promote slab formation and, still, is essential for the formation of the subduction zone.

It is clear that the above models are highly idealized:

1. Chemical and phase boundaries have not been considered; thus whole mantle convection was implied. However, in the case of upper mantle convection, adiabatic and viscous heating (with Di=0.19) in connection with olivine rheology also show a very strong tendency to concentrate the downwelling flow (H. Schmeling and G. Marquart, unpublished results on sublithospheric convection, 1989).

2. Accounting for spherical geometry would increase the temperature jump across the upper TBL on the expense of the temperature increase across the lower TBL (Zebib et al., 1980; Olson, 1981). Three-dimensional calculations on a spherical Earth (Bercovici et al., 1988) show that the downwelling takes place along long linear sheets, while the upwelling occurs in isolated broad regions. These findings justify a two-dimensional treatment of the slab problem as addressed in this study.

3. While in this study downwelling is symmetric with respect to the side boundary, all subduction zones in nature are asymmetric. Asymmetric subduction may lead to two decoupling zones adjacent to the slab of different viscosity, producing pressure fields which deflect the slab toward the low-viscosity side.

5. Conclusions

The convection calculations of this study revealed a strong interaction between a variable rheology, compression, and, in particular, adiabatic and viscous heating: upwelling plumes show a strong tendency of broadening, while the downwelling flow concentrates, being mechanically decoupled from the interior of the convection cell. This mechanism is strongest for non-Newtonian rheology. Extrapolating the results to a stronger temperature dependence of the rheology and a higher Rayleigh number, appropriate for the Earth, the decoupling is expected to occur at even smaller dissipation numbers than observed here. This kind of decoupling seems to be necessary for the formation of subducting slabs. The models predict subducting slabs to be flanked by two low-viscosity zones. These inhibit an early dispersal of downwelling material and mixing into the mantle. The increase of negative buoyancy forces with depth observed in the models may help the slabs to penetrate into the lower mantle. A concentrated downwelling and a broad, slow upwelling flow (except in mantle plumes) would also explain the long-term persistence of different chemical reservoirs in the mantle because of a low mixing rate (Loper, 1985).

Compression in the lower mantle reduces the thickness of the lower thermal boundary layer by 20-50% compared to incompressible convection, thereby increasing the mean temperature. Increasing the dissipation number in variable viscosity convection may either damp or speed up convection depending on the rheology, while constant viscosity convection is only damped by increasing Di. Geoid undulations in constant viscosity convection are virtually independent of compression for constant Di. The threshold to time-dependent variable viscosity convection is drastically reduced for internally heated convection if the anelastic liquid approximation is applied.

Acknowledgments. This work profited from stimulating discussions with U. Christensen, P. Machetel, and D. Yuen. Critical and thoughtful reviews by E. Robinson and two anonymous reviewers strongly improved the paper.

References

Anderson, D. L., A seismic equation of state, II, Shear properties and thermodynamics of the lower mantle, Phys. Earth Planet. Inter., 307-323, 1987.

Bercovici, D., G. Schubert, G. A. Glatzmaier, and J. R. Baumgardner, Three-dimensional, spherical, compressible models of whole mantle convection, paper presented at First SEDI Symposium: Structure and Dynamics of the Core and Adjacent Mantle, Sponsor NSF and NASA, Blanes, Spain, 1988.

Blankenbach, B., et al., A benchmark comparison for mantle convection codes, J. Geophys., in press, 1989.

Bott, M. H. P., The Interior of the Earth, Edward Arnold, London, 1982.

Christensen, U., Convection in a variable-viscosity fluid: Newtonian versus power-law rheology, Earth Planet. Sci. Lett., 64, 153-162, 1983.

Christensen, U., Convection with pressure- and temperature-dependent non-Newtonian rheology, Geophys. J. R. Astron. Soc., 77, 343-384, 1984.

Christensen, U., and D. A. Yuen, The interaction of a subducting lithospheric slab with a chemical or phase boundary, J. Geophys. Res., 89, 4389-4402, 1984.

Craeger, K. C., and T. H. Jordan, Slab penetration into the lower mantle beneath the Mariana and other island arcs of the Northwest Pacific, J. Geophys. Res., 91, 3573-3589, 1986.

Cserepes, L., Numerical studies of non-Newtonian

mantle convection, Phys. Earth Planet. Inter., 30, 49-61, 1982.
Davies, G. F., Role of the lithosphere in mantle convection, J. Geophys. Res., 93, 10,451-10,466, 1988.
Doornbos, D. J., Present seismic evidence for a boundary layer at the base of the mantle, J. Geophys. Res., 88, 3498-3505, 1983.
Doornbos, D. J., and J. C. Mondt, P and S waves diffracted around the core and the velocity structure at the base of the mantle, Geophys. J. R. Astron. Soc., 57, 381-395, 1979.
Dziewonski, A. M., Mapping the lower mantle: Determination of lateral heterogeneity in P velocity up to degree and order 6, J. Geophys. Res., 89, 5929-5952, 1984.
Dziewonski, A. M., and D. L. Anderson, Preliminary reference earth model, Phys. Earth Planet. Inter., 25, 297-356, 1981.
Hager, B. H., Subducted slabs and the geoid: Constraints on mantle rheology and flow, J. Geophys. Res., 89, 6003-6015, 1984.
Hager, B. H., and M. Gurnis, Mantle convection and the state of the Earth's interior, Rev. Geophys., 25, 1277-1285, 1987.
Heinz, D. L., and R. Jeanloz, Measurement of the melting curve of $Mg_{0.9}Fe_{0.1}SiO_3$ at lower mantle conditions and its geophysical implications, J. Geophys. Res., 92, 11,437-11,444, 1987.
Jacoby, W. R., Parafin model experiment of plate tectonics, Tectonophysics, 35, 103-113, 1976.
Jacoby, W. R., and H. Schmeling, Convection experiments and driving mechanism, Geol. Rundsch., 70, 207-230, 1981.
Jacoby, W. R., and H. Schmeling, On the effects of the lithosphere on mantle convection and evolution, Phys. Earth Planet. Inter., 29, 305-319, 1982.
Jarvis, G. T., and D. P. McKenzie, Convection in a compressible fluid with infinite Prandtl number, J. Fluid Mech., 96, 515-583.
Jarvis, G. T., and W. R. Peltier, Long wavelength features of mantle convection, in Mathematical Geophysics, edited by N. J. Vlaar, G. Nolet, M. J. R. Wortel, and S. A. P. L. Cloetingh, pp. 209-226, D. Reidel, Hingham, Mass., 1988.
Kincaid, C., and P. Olson, An experimental study of subduction and slab migration, J. Geophys. Res., 92, 13,932-13,840, 1987.
Kirby, S. H., Rheology of the lithosphere, Rev. Geophys., 21, 1458-1487, 1983.
Knittle, E., R. Jeanloz, and G. L. Smith, Thermal expansion of silicate perovskite and stratification of Earth's mantle, Nature, 319, 214-216, 1986.
Kopitzke, U., Finite element convection models: Comparison of shallow and deep mantle convection, and temperatures in the mantle, J. Geophys., 46, 97-121, 1979.
Loper, D. E., A simple model of whole mantle convection, J. Geophys. Res., 90, 1809-1836, 1985.
Loper, D. E., and F. D. Stacey, The dynamical and thermal structure of deep mantle plumes, Phys. Earth Planet. Inter., 33, 304-317, 1983.
Machetel, P., and D. A. Yuen, Penetrative convective flows induced by internal heating and mantle compressibility, J. Geophys. Res., in press, 1989.
Marquart, G., and H. Schmeling, Topography and geoid undulations caused by small scale convection beneath continental lithosphere of variable elastic thickness, J. Geophys., in press, 1989.
Morelli, A., and A. M. Dziewonski, Topography of the core-mantle boundary and lateral homogeneity of the liquid core, Nature, 325, 678-683, 1987.
Olson, P., Mantle convection with spherical effects, J. Geophys. Res., 86, 4881-4890, 1981.
Parmentier, E. M., D. L. Turcotte, and K. E. Torrance, Studies of finite amplitude non-Newtonian thermal convection in the Earth's mantle, J. Geophys. Res., 81, 1839-1846, 1976.
Parsons, B., and S. Daly, The relationship between surface topography, gravity anomalies, and temperature structure of convection, J. Geophys. Res., 88, 1129-1144, 1983.
Peltier, W. R., Mantle convection and viscosity, in Proceedings of the Enrico Fermi International School of Physics (Course LXXVIII), edited by A. Dziewonski and E. Boschi, North-Holland, New York, 1980.
Quareni, F., and D. A. Yuen, Mean-field methods in mantle convection, in Mathematical Geophysics, edited by N. J. Vlaar, G. Nolet, M. J. R. Wortel and S. A. P. L. Cloetingh, pp. 227-264, D. Reidel, Hingham, Mass., 1988.
Ranalli, G., Rheology of the Earth, 366 pp., Allen and Unwin, Boston, Mass., 1987.
Ricard, Y., L. Fleitout, and C. Froidevaux, Geoid heights and lithospheric stresses for a dynamic earth, Ann. Geophys., 2, 267-286, 1984.
Schmeling, H., and W. R. Jacoby, On modelling the lithosphere in mantle convection with non-linear rheology, J. Geophys., 50, 89-100, 1981.
Sclater, J. G., B. Parsons, and C. Jaupart, Oceans and continents: Similarities and differences in the mechanisms of heat loss, J. Geophys. Res., 86, 11,535-11,552, 1981.
Solheim, L. P., and W. R. Peltier, Heat transfer and mechanical mixing in a spherical axisymmetric model of mantle convection in the high Rayleigh number chaotic regime, paper presented at 17th International Conference on Mathematical Geophysics, sponsor NSF and NASA, Blanes, Spain, 1988.
Spalding, D. B., A novel finite difference formulation for differential expressions involving both first and second derivatives, Int. J. Numer. Methods Eng., 4, 551-559, 1972.
Stacey, F. D., A thermal model of the Earth, Phys. Earth Planet. Inter., 15, 341-348, 1977.
Steinbach, V., Convection in a compressible fluid with depth-dependent material properties (abstract), Eos Trans. AGU, 68, 1447, 1987.
Turcotte, D. L., A. T. Hsui, K. E. Torrance, and G. Schubert, Influence of viscous dissipation on Benard convection, J. Fluid Mech. 64, 369-374, 1974.
Williams, Q., R. Jeanloz, J. Bass, B. Svendsen, and T. J. Ahrens, The melting curve of iron to 250 gigapascals: A constraint on the temperature at the Earth's center, Science, 236, 181-182, 1987.
Yuen, D. A., and S. Zhang, Equation of state and rheology in deep mantle convection, in Perovskite: A Structure of Great Interest to

Geophysics and Materials Sciences, Geophys. Monogr. Ser., vol. 45, edited by A. Navrotsky and D. Weidner, pp. 131-146, AGU, Washington, D.C., 1989.

Yuen, D. A., F. Quareni, and H.-J. Hong, Effects from equation of state and rheology in dissipative heating in compressible mantle convection, Nature, 326, 67-69, 1987.

Zebib, A., G. Schubert, and J. M. Straus, Infinite Prandtl number thermal convection in a spherical shell, J. Fluid Mech., 97, 257-277, 1980.

Zhang, S., and D. A. Yuen, Deformation of the core-mantle boundary induced by spherical-shell, compressible convection, Geophys. Res. Lett., 14, 899-902, 1987.

Zhang, S., and D. A. Yuen, Dynamic effects on the core-mantle boundary from depth-dependent thermodynamical properties of the lower mantle, Geophys. Res. Lett., 15, 451-454, 1988.

Zhao, W., and D. A. Yuen, The effects of adiabatic and viscous heating on plumes, Geophys. Res. Lett., 14, 1223-1226, 1987.

H. Schmeling, Hans Ramberg Tectonic Laboratory, Geological Institute, Box 555, 751 22 Uppsala, Sweden

(Received August 11, 1988;
revised February 15,
accepted March 16, 1989.)